Patient-Specific Model Generation and Simulation for Pre-Operative Surgical Guidance for Pulmonary Embolism Treatment

Shankar P. Sastry, Jibum Kim, Suzanne M. Shontz, Brent A. Craven, Frank C. Lynch, Keefe B. Manning, and Thap Panitanarak

Abstract Pulmonary embolism (PE) is a potentially-fatal disease in which blood clots (i.e., emboli) break free from the deep veins in the body and migrate to the lungs. In order to prevent PE, anticoagulation therapy is often used; however, for some patients, it is contraindicated. For such patients, a mechanical filter, namely an inferior vena cava (IVC) filter, is inserted into the IVC to capture and prevent emboli from reaching the lungs. There are numerous IVC filter designs, and it is not well understood which particular IVC filter geometry will result in the best clinical outcome for a given patient. Patient-specific computational fluid dynamic (CFD) simulations may be used to aid physicians in IVC filter selection and placement. In particular, such computational simulations may be used to determine the capability of various IVC filters in various positions to capture emboli, while not creating additional emboli or significantly altering the flow of blood in the IVC. In this paper, we propose a computational pipeline that can be used to generate patient-specific geometric models and computational meshes of the IVC and IVC filter for various IVC anatomies based on the patient's computer tomography (CT) images.

Shankar P. Sastry
The Pennsylvania State University, e-mail: sps210@cse.psu.edu

Jibum Kim
The Pennsylvania State University, e-mail: jzk164@cse.psu.edu

Suzanne M. Shontz
The Pennsylvania State University, e-mail: shontz@cse.psu.edu

Brent A. Craven
Penn State Applied Research Laboratory, e-mail: bac207@psu.edu

Frank C. Lynch
Penn State Milton S. Hershey Medical Center, e-mail: flynch@hmc.psu.edu

Keefe B. Manning
The Pennsylvania State University, e-mail: kbm10@psu.edu

Thap Panitanarak
The Pennsylvania State University, e-mail: txp214@cse.psu.edu

Our pipeline involves several steps including image processing, geometric model construction, surface and volume mesh generation, and CFD simulation. We then use our patient-specific meshes of the IVC and IVC filter in CFD simulations of blood flow, whereby we demonstrate the potential utility of this approach for optimized, patient-specific IVC filter selection and placement for improved prevention of PE. The novelty of our approach lies in the use of a superelastic mesh warping technique to virtually place the surface mesh of the IVC filter (which was created via computer-aided design modeling) inside the surface mesh of the patient-specific IVC, reconstructed from clinical CT data. We also employ a linear elastic mesh warping technique to simulate the deformation of the IVC when the IVC filter is placed inside of it.

1 Introduction

Venous thromboembolic disease is a process that begins with blood clot formation in the legs known as deep vein thrombosis (DVT). If left untreated these blood clots can progress and eventually migrate to the lungs, causing a pulmonary embolism (PE). The progression of venous thromboembolic disease from DVT to PE is often asymptomatic, but once PE occurs, it is associated with high morbidity and mortality. Over 10% of patients with acute PE die in the first hour. If not adequately treated, the overall mortality of PE is over 30%. The incidence of pulmonary embolism in the United States is estimated to be over 600,000 cases per year. Approximately 200,000 deaths are attributed to pulmonary embolism in the United States annually [6].

Both the occurrence of DVT and its progression to PE can be prevented with the use of anticoagulants, medications that prevent blood from clotting. However, anticoagulant carries with it the risk of bleeding complications. There are patients who cannot receive anticoagulation therapy because of comorbid factors that put them at increased risk for bleeding complications or for whom anticoagulation has failed to prevent the occurrence or progression of DVT. As an alternative to anticoagulation therapy, these patients often undergo implantation of a device known as an inferior vena cava filter (IVC filter) (Figure 1).

IVC filters are mechanical devices that are placed into the IVC using percutaneous catheter based techniques. The IVC filter functions as a mechanical barrier that can capture large clots and prevent them from reaching the lungs. Most DVT occurs in the legs and pelvis. Since the inferior vena cava (IVC) is the common venous pathway that drains the majority of blood from the lower half of the body, it makes sense to place a barrier there since it is the common route that any blood clot must traverse in order to reach the lungs.

While clinical studies have shown that IVC filters are effective in preventing PE, especially during the period shortly after they have been placed [18], PE still occurs in up to 5% of the cases, despite the presence of an IVC filter [38]. Experiments designed to study the factors that determine the clot trapping efficiency of IVC fil-

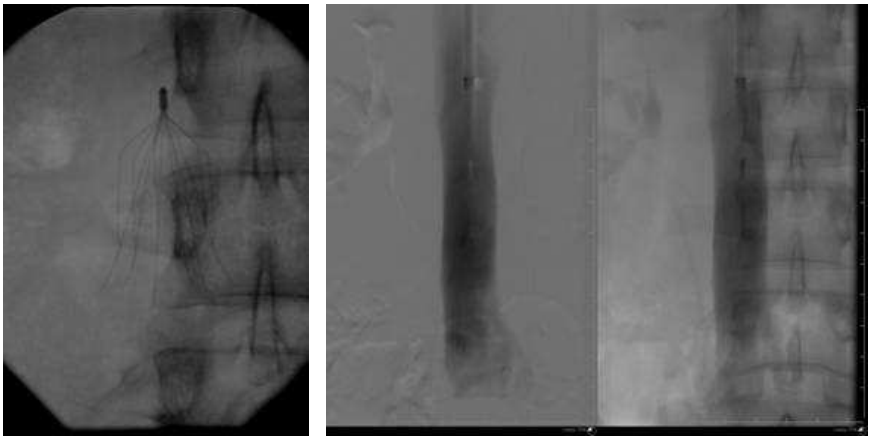

(a) (b)

Fig. 1 X-ray image (left) and digital subtraction angiography (right) of a G2 filter (Bard Peripheral, Phoenix AZ) in the inferior vena cava.

ters have largely focused on device design. Little attention has been given to other factors that might affect IVC filter effectiveness, which include the size and shape of the cava, anatomic variations of the IVC and its tributaries, the site of IVC filter implantation, and the effect of respiratory variation in caval size and blood flow.

The IVC is the dominant venous structure in the abdomen. It is generally oval in shape with a major axis measuring between 14 and 33 mm. It is formed as the confluence of the right and left common iliac veins at approximately the level of the fourth lumbar vertebral body. The largest tributaries are the single left and right renal veins that typically enter the IVC at the level of the first lumbar segment. Typically, IVC filters are placed in the infrarenal IVC, that segment of the IVC between the confluence of the iliac veins and the insertion of the renal veins. Filters are placed here so that clots captured in the filter do not propagate back into the renal veins and cause renal failure.

A high degree of anatomic variability is seen in the human infrarenal IVC. Structural anatomic variants of the infrarenal IVC are common and have been well described in the literature [82] (Figure 2). Duplication of the infrarenal IVC occurs 1-3% of the time. In this case, the second IVC drains into the left renal vein. While the two infrarenal IVCs may be equal in size, the variant represents a spectrum of differences in caval anatomy. In the extreme case, the right infrarenal IVC is entirely absent leaving only a left-sided IVC. This occurs in 0.2-0.5% of patients.

Anatomic variations of the renal veins also greatly impact IVC anatomy and therefore affect IVC filter placement and function [82]. While duplication of the right renal vein has a relatively minor impact on caval anatomy, duplication of the left renal vein usually results in one renal vein that passes anterior to the aorta and one that passes posterior to the aorta. This circumaortic left renal vein occurs in

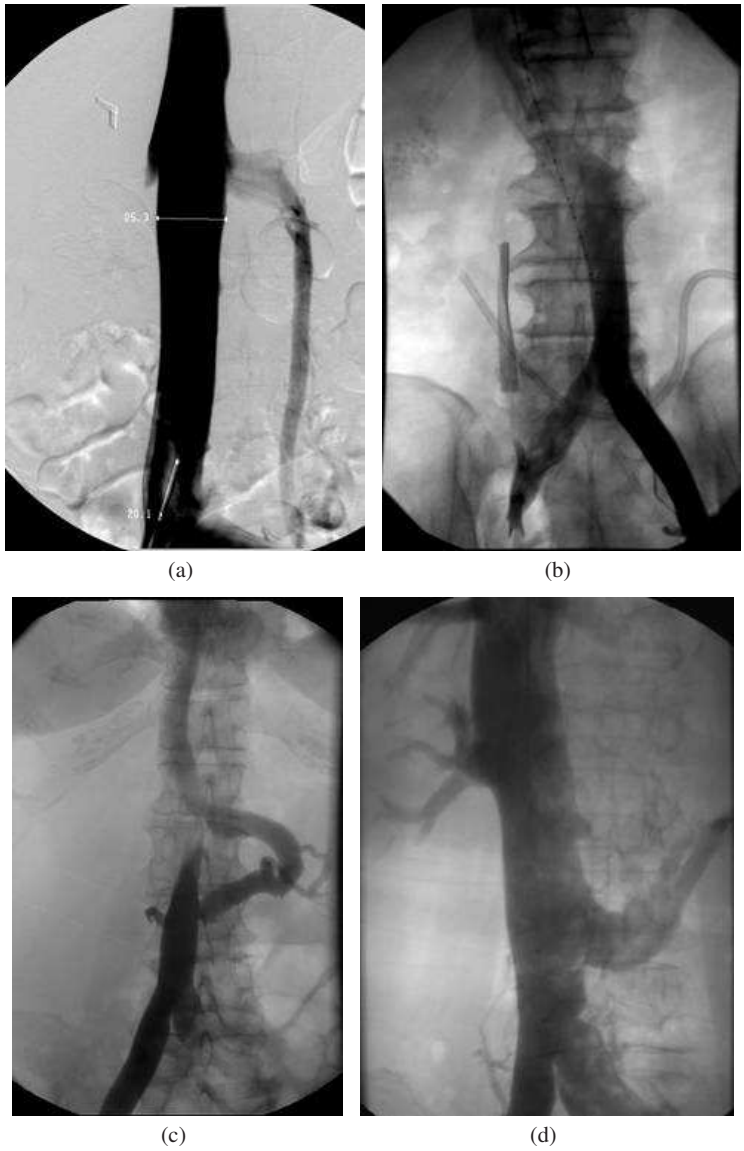

Fig. 2 Common IVC/renal vein variants: (a) duplicated IVC, (b) left sided IVC, (c) circumaortic left renal vein, (d) retroaortic left renal vein.

up to 9% of patients, and in its extreme form, which occurs in approximately 3% of patients, only the retroaortic left renal vein is present. These variants are significant because the retroaortic vein inserts into the IVC much more caudally, greatly shortening the effective length of the infrarenal IVC (Figure 2).

These variations in infrarenal IVC size and anatomy may significantly impact IVC filter function. IVC filters are generally designed with self expanding filter elements that become constrained against the caval wall. This "one size fits all" approach leads to instances where the clot trapping elements of the filter are more closely aligned in cavae of smaller cross sectional area (Figure 3). Variations in branch anatomy may lead to different flow patterns that significantly affect how a clot is presented to the IVC filter, potentially influencing the chances that it is captured. Abnormalities of the spine may lead to curvature or angulation of the infrarenal IVC. Even in cases of "usual" caval size and anatomy, the location of filter implantation (high or low in the IVC) may impact its ability to capture clots. Blood flow through a filter as well as its ability to capture clots also changes as clots accumulate in the filter.

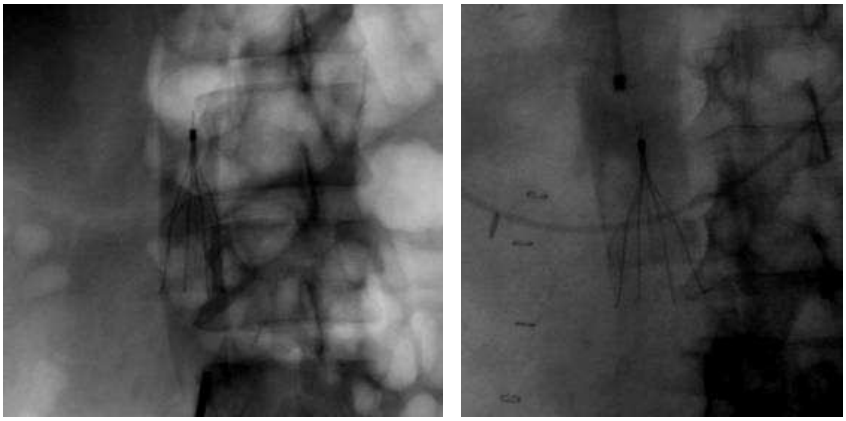

(a) (b)

Fig. 3 Celect IVC filters (Cook, Bloomington IN) placed in a 15 mm diameter cava (left) and a 26 mm diameter cava (right). In the smaller diameter cava, the filter elements are more closely compressed, potentially leading to a higher clot trapping efficiency.

Historically, information regarding the clot trapping effectiveness of IVC filters has been derived from *in vivo* animal studies [10, 32, 37, 54] and increasingly from *in vitro* modeling [14, 37, 54, 71]. However, information derived by these means is limited by several factors. Animal studies typically involve a small number of subjects and are performed in species where IVC anatomy and size only approximate that of humans. Real time evaluation of blood flow characteristics in animal models is difficult or impossible given that methods to measure flow characteristics tend to be optically based, requiring an optically clear caval wall and blood. Evaluation of clot trapping in live animal models usually requires the creation and use of radiopaque thrombi, which must be observed using radiographic techniques.

In vitro experiments are typically performed by placing the filter in a Silastic or Plexiglas tube, which is then perfused with a medium that approximates the fluid

characteristics of blood. These models are limited since they are based on an idealized IVC that lacks the biomechanical properties, anatomic variation, respiratory variation in size, and flow disturbances from branch vessels that are seen in actual human IVCs. Until recently, evaluation of flow characteristics and clot trapping efficiency has been based on subjective observations, such as observations made when artificially created thrombi are introduced into the flow model.

Given the sheer number of combinations of the factors discussed, exhaustive modeling of all possibilities by *in vivo* and *in vitro* techniques is impractical. However, computational modeling has been one approach to overcome this and other limitations of *in vivo* and *in vitro* experimentation. Several papers have been written to date concerning computational fluid dynamic (CFD) studies of the flow characteristics of various combinations of the IVC, IVC filter, and blood clots [56, 68, 69, 70, 72, 73, 78]. An important limitation of the majority of these studies is the simplistic and unrealistic geometric modeling of the IVC with the exception of [56]. In their paper, Moore *et al.* employ a realistic, compliant model to represent the IVC, its branching vessels (including the iliac and renal veins), and lumbar curvature based on an average of the normal IVC anatomy of a patient. In addition, none of these studies examined the impact of anatomic IVC variant on the flow results. Simplistic, idealized geometric models of the blood clots were all used in all of these CFD studies. In contrast, accurate models of the IVC filters are used in each of the studies with the exception of [56], which studied only the realistic IVC model in conjunction with blood clots.

Accurate anatomic models of normal and variant IVCs combined with accurate models of IVC filters can be used for CFD studies, providing a tool that can then be used to make predictions about the flow characteristics, biological response, and clot trapping ability of a given IVC filter design across a wide range of anatomic and physiologic variables. Predictions about differences in clot trapping ability of various filter designs, deployment locations, and deployment configurations might also be derived with the technique. Finally, CFD studies on anatomically correct models could also prove useful in the development of novel IVC filter designs.

The rest of the paper is organized as follows. In Section 2, we describe the state-of-the-art techniques for patient-specific mesh generation for use in CFD simulations. In Section 3, we describe our previous attempts at generating accurate geometric models of the IVC and the IVC filter using only computer tomography (CT) images as input. In Section 4, we describe our computational pipeline for generating geometric models and computational meshes of the IVC and IVC filter and performing CFD simulations of blood flow. In Section 5, we present our results on generation of patient-specific meshes for various IVC anatomies. We also present our results from the CFD simulations of blood flow in which use our patient-specific meshes. Conclusions and some directions for future research are presented in Section 6.

2 Generation of Patient-Specific Meshes for CFD Simulations

Generation of patient-specific meshes for CFD simulations from medical images (e.g., CT, MRI, etc.) usually follow a computational pipeline approach (e.g., [9, 11, 39]). The computational pipeline typically involves many of the following steps [17]: (1) segmentation of the medical image; (2) modeling of invisible structures (if applicable); (3) surface mesh generation; (4) volume mesh generation; (5) optimization of the mesh. The main criteria for computational meshes generated via this pipeline to satisfy are: mesh validity, geometric accuracy, smoothness and resolution control, and adequate mesh quality. Below we summarize state-of-the-art techniques for Steps 1 and 3-5 in the above pipeline, as these steps are the most relevant to our proposed research.

2.1 Image Segmentation

Region growing methods [29] and level-set methods [59] are two popular approaches for segmentation of medical images [53]. Region growing methods require an initial seed to be manually chosen and extract a region connected to the seed by growing until predefined criteria (such as intensity information or edges in images) [29] are met; however, they are sensitive to noise. Level-set methods are techniques for delineating region boundaries using closed parametric curves (or surfaces) that deform under the influence of a PDE; however, they require initial input. Region-growing methods can be combined with level-set methods to obtain initial and improved medical image segmentations, respectively (e.g., [28]).

2.2 Surface Mesh Generation

The classical approach for generating computational meshes from segmented medical images has been to perform a surface interpolation between the contours describing the segmented volume [23, 55, 58]. Several researchers have used the marching cubes algorithm [43] or one of its improvements [26, 30, 15, 16, 33] to create an initial surface mesh from the 3D segmented data set. The marching cube method is fast and relatively simple, but may not generate a topologically-consistent surface mesh. This limitation was removed in the regularized marching tetrahedron (RMT) algorithm [75].

Virtual implantation of a medical device into a patient anatomy has also been used to create patient-specific geometric models of implanted stents [27]. In this technique, a series of Boolean operations are performed in order to implant the stent geometry into the patient anatomy, yielding an embedded surface.

2.3 Volume Mesh Generation

Numerous researchers have developed techniques for generating computational volume meshes for use in biomedical simulations. Typically, finite element or finite volume simulations are performed using tetrahedral [17, 25, 34, 74, 80] or hexahedral volume meshes [60, 77, 81]; although hybrid meshes [22, 49, 79] represent a trade-off between the higher accuracy of hexahedral meshes and the ease of generation of tetrahedral meshes.

Dynamic mesh generation is the problem of maintaining a mesh for a geometric domain whose shape changes, e.g., as a function of time. Various techniques, such as mesh warping or adaptivity can be used to update the mesh as the domain deforms. Mesh warping (or morphing) is the process of determining a one-to-one transformation which maps the original 3D mesh to a target domain specified by its boundary surface. Several biomedical mesh warping algorithms have been developed (e.g., [7, 8, 40, 48, 62, 64, 65, 66, 67, 81]). Typically the mesh topology is maintained throughout the mesh warping process; however, moving mesh techniques employing adaptive mesh refinement [51, 52] have been used when topological changes occur in the domain.

2.4 Mesh Optimization

Recent research has shown the importance of performing mesh quality improvement before solving PDEs in order to: improve the condition number of the linear systems being solved [61], reduce the time to solution [24], and increase the accuracy of the partial differential equation (PDE) solution. Therefore, mesh optimization methods are often used to obtain high-quality biomedical meshes [31, 42, 76] for numerical modeling and simulation. Only recently have mesh optimization techniques been designed for improving the quality of hybrid biomedical meshes. Dyedov et al. [22] recently introduced a variational approach for smoothing prismatic boundary-layer meshes based on improving triangle shape and edge orthogonality in prism elements; their smoothing approach is based upon their scaled aspect ratio prism mesh quality metric, which is one of only two such metrics in the literature [19].

2.5 Motivation for Current Study

Despite all of the research that has been performed to date in image processing and dynamic mesh generation, there is no computational pipeline or algorithm for generation of anatomically-accurate, patient-specific computational meshes of an IVC filter implanted in the IVC for use in CFD simulations of blood flow. Thus, in this chapter, we focus on the development of such a computational pipeline.

3 Patient-Specific Geometric Modeling of an IVC Filter Implanted in the IVC

A high-resolution geometric model of an IVC filter is necessary for generation of an accurate geometric model of an IVC filter implanted in an anatomically-accurate, patient-specific IVC model. The use of such a model will permit accurate CFD simulations of blood flow on the IVC models. Thus, although a completely image-based technique for geometric modeling of the IVC, its surrounding veins, and the IVC filter may seem desirable, in this section, we illuminate the difficulties experienced in trying to generate such a high-resolution model solely from patient CT images.

An example of an IVC filter is shown in Figure 4(a). The challenge in generating a high-resolution model of such an IVC filter lies in extracting it from relatively low-resolution clinical CT images. This is particularly difficult for the following reasons: (1) the IVC filter is composed of extremely thin Nitinol wires (approximately 0.2mm in diameter); (2) a radiologist typically acquires a low-resolution CT scan of the patient after filter implantation to minimize radiation exposure; (3) beam hardening artifacts distorts the wires in the CT images. Consequently, using the IVC filter extracted from patient CT images results in a low-resolution IVC filter model (Figure 4(b)), which is unrealistic in size and shape (i.e., it is too thick, and the geometry is underresolved), and leads to unrealistic obstruction of the IVC in the blood flow simulation.

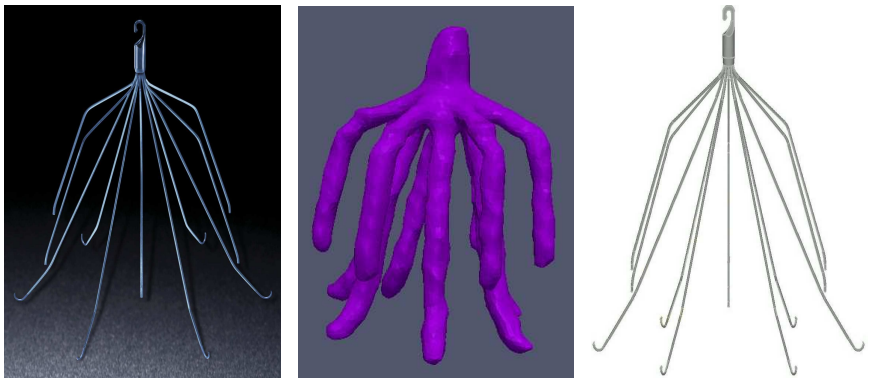

(a) (b) (c)

Fig. 4 Initial, unsuccessful attempts at creating high-resolution IVC filter models from CT data alone, illustrating the shortcomings of this approach: (a) G2 Express IVC filter (Bard Peripheral, Tempe, AZ), (b) low-resolution IVC filter model (created from a low-resolution patient CT scan), which would result in a severely-obstructed IVC if virtually implanted, (c) high-resolution IVC filter model (created via CAD)

Initial, unsuccessful attempts at creating high-resolution models of the IVC filter have included: (1) segmentation of higher-resolution CT images of an idealized model (i.e., one constructed for performing *in vitro* experiments), (2) modification of the low-resolution IVC model using surface offsetting methods, and (3) skeletonization of the low-resolution IVC filter model. Segmentation of the higher-resolution CT images resulted in an IVC filter model which was somewhat improved in terms of size but was still too thick, as the IVC filter arms/legs were still inadequately resolved. Modification of the original low-resolution IVC filter model by surface offsetting techniques led to a thinner, but still unrealistic IVC filter model in terms of the geometry. The skeletonization approach also led to a thin IVC filter model with unrealistic geometry. Thus, more sophisticated techniques are needed for creation of a high-resolution IVC filter model to be virtually implanted in a patient's IVC. Consequently, to obtain a high-resolution model of the IVC filter, we propose a virtual filter implantation technique, whereby a high-resolution IVC filter model created using computer-aided design (CAD) (Figure 4(c)) is implanted into the IVC using mesh warping techniques.

4 A Combined CAD- and CT Image-Based Model Creation Technique for CFD Simulations of Blood Flow in Patient-Specific Models

In this section, we describe our computational pipeline for generation of patient-specific geometric models and computational meshes of the IVC and IVC filter, suitable for use in CFD simulations of blood flow.

Our computational pipeline consists of several steps. The process begins with *acquisition* and then *segmentation* of a patient's CT images in order to obtain a geometric model of the patient's IVC and its adjacent veins such as the renal and iliac veins. A surface mesh is then generated on the geometry using the marching cubes algorithm. The *surface mesh generation* step is followed by *surface reconstruction* and *smoothing* resulting in an optimized surface such as is required for subsequent volume mesh generation. A geometric model (i.e., a CAD model) of the IVC filter is then *generated* and *virtually placed* in the IVC at an appropriate location specified by a vascular surgeon or at the location observed in the CT images. Superelastic and linear elastic constitutive laws are used to simulate the deformations of the IVC filter and the IVC, respectively. In particular, the IVC surface mesh and IVC filter volume mesh are warped using these constitutive laws. A *volume mesh* with properties suitable for CFD simulations, i.e., with high-quality boundary layer elements, is then generated on this anatomically-accurate, patient-specific geometry. The final step is to perform *CFD simulations* of the blood flow using the high-fidelity volume mesh of the IVC and IVC filter.

We now describe each step in our computational pipeline in more detail.

4.1 Image Acquisition

The first step in our computational pipeline is image acquisition. After obtaining Institutional Review Board exemption, two sets of CT images representing different IVC anatomies were obtained from a retrospective review of patient records. In particular, the CT images obtained for use in this study represent the left and retroaortic IVC anatomies. The CT image data sets have 0.87 mm/pixel in-plane resolution and a 1.5 mm out-of-plane resolution. In addition, we designed an idealized IVC model based on a normal IVC anatomy. A data set of high-resolution CT images were obtained using a multi-slice spiral CT scanner for our idealized IVC model. The image data set has a 0.44 mm/pixel in-plane resolution and a 0.6 mm out-of-plane resolution.

4.2 Image Segmentation

The second step of our pipeline is segmentation of the patient's CT images; this is done in order to determine the geometry of the patient's IVC. In our study, image segmentation is a semi-automatic process in which we mark the regions corresponding to IVC and its adjacent veins in each 2D CT image in order to obtain an accurate geometry. The regions are then extracted using one of the algorithms described below, which are implemented in Amira [4], an image segmentation software package.

4.2.1 Region Growing

The region growing technique [29] takes a medical image and seeds as input, where each seed denotes a region that needs to be segmented. The seeds are progressively grown from one pixel to the neighboring pixels based on the pixel intensity and its distance from the seed pixel.

4.2.2 Gradient-Based Region Growing

The gradient-based region growing technique, as implemented in Amira, is similar to the region growing technique. The difference is in the stopping criteria used to terminate the progressive growth of the regions. In the former case, termination was based on the intensity of the pixels. In the latter case, it is based on the magnitude of the gradient of the pixel intensity [5]. The gradient of the pixel intensity is given by

$$G = \sqrt{I_x^2 + I_y^2},$$

where I_x and I_y are the partial derivatives of the image intensity with respect to the horizontal and the vertical direction, respectively.

4.2.3 Intelligent Scissors

The intelligent scissors algorithm [46] constructs an underlying graph for an image in which the pixels are interpreted as nodes and adjacent pixels are connected by edges. As the gradient of the magnitude of the pixel intensity is an excellent edge indicator for medical image segmentation, the weight of the edges is a function of the gradient of the magnitude of the pixel intensity between two adjacent pixels. In order to enable the shortest path between each pair of pixels to correspond to edges in the images, the gradients are scaled so that a high gradient results in lower edge cost. The intelligent scissors algorithm finds the shortest path between a set of user-chosen pixels using Dijkstra's algorithm. An ordered set of pixels whose shortest paths from one pixel to the next one form a closed loop successfully completes the segmentation of an image. This technique is used to segment patient images when the other techniques failed due to image noise.

4.3 Surface Mesh Generation

After the geometry of the IVC and its adjacent veins are extracted using one of the above segmentation algorithms, a surface mesh of their geometry is generated using the marching cubes algorithm in Amira. The surface mesh which is generated by this algorithm is often not of good quality and hence often needs to be smoothed before being used for further computational analysis. If the surface mesh is overrefined, it may also need to be coarsened before smoothing.

4.3.1 Marching Cubes

The marching cubes algorithm [26, 30, 43] constructs a triangular surface mesh from segmented images by evaluating the pixels from multiple images and determining the optimal triangulation that best describes the isosurface obtained from the segmented images. The pixels from multiple images form imaginary cubes, where each pixel represents each vertex of the cubes. Each pixel is deemed either inside the region of interest (i.e., inside either the IVC or its adjacent veins) or outside the region of interest. For a set of eight pixels forming a cube, this results in $2^8 = 256$ possible combinations for the cube. Due to symmetry, the number of combinations can be reduced to around 15. Every cube is evaluated to find the combination to which the configuration reduces, and a topologically-consistent triangulation is constructed based on the configuration to obtain a triangular surface mesh.

4.3.2 Poisson Surface Reconstruction

For the idealized IVC model, the surface mesh of the IVC and the adjacent veins obtained from the marching cube algorithm was overrefined. Thus, the mesh was be simplified before using it for further analysis. For this purpose, we use the Poisson surface reconstruction approach [44], which has been implemented in Meshlab [45]. Here, an indicator function is constructed, whose value is 1 inside the surface or 0 outside the surface. Since this function is discontinuous, the indicator function is convolved with a smoothing function, and the gradient of the resulting function, $\mathbf{V}$, is computed. In order to reconstruct the surface using the gradient, a function, χ, is computed such that it gradient is equal to the vector field, i.e.,

$$\nabla\chi = \mathbf{V},$$

where ∇ is a gradient operator. Applying the divergence operator on both sides, we obtain

$$\Delta\chi = \nabla \cdot \mathbf{V}.$$

In order to solve the Poisson system, an adaptive octree mesh of the surface mesh is constructed such that there is a greater resolution near the original surface mesh. After solving the Poisson equation with Neumann boundary conditions, a coarser surface mesh is constructed using the solution.

4.3.3 Surface Mesh Smoothing

The image segmentation and surface reconstruction steps are usually affected by image noise. Construction of volume meshes using noisy surface meshes results in failure of the mesh generator or in poor quality meshes for CFD simulations. Thus, the surface meshes must be smoothed before they are used to generate a volume mesh of the IVC and IVC filter. Because the naive implementation of the Laplacian smoothing algorithm results in the reduction of the volume of the models, we use the Humphrey's Classes (HC) Laplacian smoothing algorithm [35] implemented in Meshlab to smooth our surface meshes. Unlike the Laplacian smoothing algorithm, the HP-Laplacian smoothing algorithm preserves the volume of the surface meshes during smoothing [35].

We briefly summarize the HP-Laplacian smoothing algorithm as follows. First, we define some notation. Let the original mesh vertices be denoted by vector $\mathbf{o}$, and let o_i denote the coordinates of the i^{th} vertex in the mesh. Let vector $\mathbf{q}$ denote the mesh vertex positions prior to the beginning of the current iteration. Now define vector $\mathbf{p}$ to be the new vertex positions after the current iteration. In the HC-Laplacian algorithm, the modified vertices, represented by vector $\mathbf{p}$, are first computed by Laplacian smoothing. They are then pushed back towards their original positions, vector $\mathbf{o}$, or their positions from the previous iteration, i.e., vector $\mathbf{q}$, by taking the average of the differences between their original positions and their positions in their previous iteration as shown:

$$b_i = p_i - (\alpha o_i - (1-\alpha)q_i), \text{ i.e., by}$$

$$d_i = \beta b_i - \frac{1-\beta}{|\text{adj}(i)|} \sum_{j \in \text{adj}(i)} b_j,$$

where $\text{adj}(i)$ is the set of vertices adjacent to vertex i and d_i is the vector by which the vertex p_i is pushed back. In the final step of the algorithm, the final positions,

$$p_i^{\text{final}} = p_i - d_i,$$

are computed.

4.4 Generation of a Geometric Model of the IVC Filter

The next step in our pipeline is to generate a geometric model of the IVC filter. We obtained a Computer-Aided Design (CAD) model of the G2 Express IVC filter, which was generated using the Siemens NX 6 software package [63], from Rick Schraf and Todd Fetterolf for use in our study.

4.5 Virtual IVC Filter Placement

The subsequent step in the pipeline is to virtually place the geometric model of the IVC filter (i.e., the CAD model) inside the IVC by simulating the bending of the filter arms and legs which occur during the IVC filter insertion procedure using finite element modeling and a superelastic constitutive law. We simulate the resulting deformation of the IVC based on a linear elastic constitutive law. We now describe the two-step process of setting up the forces to compress the filter and then releasing the forces until the filter arms and legs touch the walls of the IVC, which then slightly deforms the IVC.

4.5.1 Superelasticity-Based Mesh Warping

The arms and legs of the IVC filter are made from nitinol wires; nitinol is a superelastic material [21]. Nitinol is a shape memory alloy [20], i.e., it can revert back its original shape after undergoing large deformations. Such materials are also used to manufacture stents, which are used to dilate constricted blood vessels. Nitinol also has applications in orthodontics [50].

In order to simulate the mechanical behavior of the IVC filter during IVC filter insertion procedure, the undeformed filter is first moved to a location recommended by a physician or to the location observed in the patient's CT images. Since the IVC's diameter is smaller than the IVC filter's diameter, in our numerical model,

the IVC filter wires protrude out of the IVC surface mesh after this step has been performed. Cylindrically-inward forces are then applied on each of the arms and legs of the IVC filter in order to compress it so that it completely fits inside the IVC. In the next step, the forces are reduced until the IVC filter legs become close to the IVC walls.

This two-step process is necessary because the stress versus strain curve for the loading and unloading of nitinol follow different paths. During the IVC filter insertion procedure, the IVC filter is first compressed and is then fed into a thin tube called a deployment sheath. The sheath as well as the IVC filter are then inserted into the body either through the groin or the neck and are guided into place in the IVC. The IVC filter is then released at the desired location inside the IVC. Our two-step process mimics the loading and unloading processes acting on the IVC filter during the procedure. The forces on the filter legs in the IVC are used to deform the IVC.

Abaqus [1] was used to perform the finite element modeling for virtual filter placement of the IVC filter surface mesh inside the IVC. Numerical models for nitinol and the constitutive law for superelasticity which we employ are implemented in Abaqus. Nitinol's superelastic behavior is implemented in the Nitinol Umat subroutine in Abaqus [2]. The model is based on the uniaxial behavior of a thin nitinol wire. Table 1 shows the values of the parameters used as input to the Umat subroutine in Abaqus. These values were obtained from [13]. The deformation of the IVC filter is modeled using a superelastic constitutive law [57].

Parameter	Description	Value
E_A	Austenite elasticity	35877 MPa
ν_A	Austenite Poisson's ratio	0.33
E_M	Martensite elasticity	24462 MPa
ν_B	Martensite Poisson's ratio	0.33
e^L	Transformation strain	0.0555
$(\partial\sigma/\partial T)_L$	Loading	6.7
σ_L^S	Start of transformation loading	489 MPa
σ_L^E	End of transformation loading	572 MPa
T_0	Temperature	37^o C
$(\partial\sigma/\partial T)_U$	Unloading	6.7
σ_U^S	Start of transformation unloading	230 MPa
σ_U^E	End of transformation unloading	147 MPa

Table 1 Values of the parameters for the superelastic material properties of nitinol [57]

4.5.2 Linear Elasticity-Based Mesh Warping

It has been observed in some patients that the circular or elliptical cross-section of the IVC deforms into a hexagonal cross-section upon insertion of the IVC filter due to the forces applied by the deformed filter. Once the IVC filter mesh is virtually

warped to be completely inside the IVC, the IVC is deformed based on the forces acting on the filter. The forces on the IVC filter are cylindrically inward, and, thus, the forces on the IVC are of the same magnitude but are cylindrically outward. The vein surface vertices on which the forces are applied are chosen such that they are close to the filter vertices with which they are most likely to come in contact. Once the deformation of the vertices is obtained, we use the final vertex positions to create the volume mesh for the CFD simulations of blood flow.

Abaqus was also used for numerical modeling of the deformation of the IVC. For modeling the IVC's linear elastic behavior, we used a value of $E = 2.6 * 10^6 \text{dyn/cm}^2$ for the Young's modulus of the IVC. This value corresponds to the Young's modulus of an artery [36], which we used since its value has not yet been determined for a vein.

A surface interaction module is present in Abaqus in which it is possible to detect and impose conditions on contact interaction between the surfaces of the IVC filter and the IVC. We have found that the numerical solvers in Abaqus fail to converge when this module is used for our specific application. Because the module also failed to provide an accurate solution for modeling force interaction between a stent and a blood vessel in [13], we modified our computational technique so that the IVC filter legs come close to the IVC wall but do not come in contact with it. This was necessary in order to obtain convergence of the solvers. However, the CFD results should not be significantly affected by this modification because the distance between the IVC filter legs and the IVC wall is minimal.

4.6 Volume Mesh Generation

The next step in the computational pipeline is generation of the volume mesh using the surface meshes obtained from the above steps. We generate a volume mesh outside of the IVC filter and inside the walls of the IVC and its surrounding veins. As blood cannot flow into the surface of the filter wall, a volume mesh of the IVC filter is not needed for our CFD analysis (however; for fluid-structure interaction problems, a volume mesh of the filter may be necessary). The AFLR3 software package [3] allows us to generate such meshes using the advancing front technique with local reconnection, which we explain below.

4.6.1 Advancing Front Technique

The advancing front technique [41] generates a volume mesh from a valid surface mesh of the computational domain. A front, which is defined as a set of 2D elements, propagates from the boundary of the computational domain (i.e., its surface mesh) towards its interior. As the front propagates, volume elements are generated and are added to the volume mesh. AFLR3 generates prismatic elements on the boundary and pyramidal and tetrahedral elements elsewhere in the domain. The distance by

which the front propagates inward from the surface mesh is controlled by setting the initial distance and increasing it geometrically. Boundary layers are also generated in the mesh near the IVC walls in order to obtain physically-accurate CFD simulations of the blood flow in these areas.

4.7 Computational Fluid Dynamics

Given a high-fidelity volume mesh, the final step in the computational pipeline is the simulation of blood flow in the patient-specific IVC model using CFD. Depending on the problem of interest, steady or unsteady, laminar or turbulent calculations may be carried out. In this study, the open-source computational continuum mechanics library OpenFOAM [47] was utilized to simulate steady, laminar blood flow through the IVC. Blood was assumed to behave as a Newtonian fluid with a kinematic viscosity of 4.4 cSt. The flow rate in each renal and iliac vein was specified as 0.75 L/min and 0.6 L/min, respectively, yielding infrarenal and suprarenal IVC flow rates of 1.2 L/min and 2.7 L/min, respectively [12].

The semi-implicit method for pressure linked equations (SIMPLE) algorithm was used to solve the incompressible continuity and Navier-Stokes equations, i.e.,

$$\nabla \cdot \mathbf{u} = 0$$

$$\frac{\partial \mathbf{u}}{\partial t} + \mathbf{u} \cdot \nabla \mathbf{u} = -\frac{\nabla p}{\rho} + \nu \nabla^2 \mathbf{u}.$$

Iterative convergence of the SIMPLE solver was guaranteed by forcing the solution residuals to be less than approximately 10^{-4}. Additionally, various solution variables were monitored throughout the simulation to ensure convergence of the computed result. Computations were performed on 120 processors of a high-performance parallel computer cluster at Penn State, each simulation requiring approximately 6 h of wall clock time to obtain a converged solution.

Our computational pipeline is summarized in Algorithm 1.

5 Results from our Computational Pipeline

In the previous section, we described our computational pipeline for generation of high-fidelity, patient-specific volume meshes of the IVC anatomy and the IVC filter and CFD simulation of blood flow on these meshes. In this section, we discuss the results we obtained from each step in the pipeline.

Algorithm 1 The computational pipeline to generate patient-specific volume meshes of the IVC and IVC filter from patient CT images and a CAD model of the IVC filter and to perform CFD simulations of blood flow on them

1: Acquire patient CT images
2: Segment each patient CT image using one of the following image segmentation techniques:
   - Region growing
   - Gradient-based region growing
   - Intelligent scissors
3: Generate the surface mesh using the marching cubes algorithm.
4: **if** the surface is overrefined **then**
5: Coarsen the mesh using the Poisson surface reconstruction algorithm.
6: **end if**
7: Smooth the mesh using the HC-Laplacian smoothing algorithm.
8: Generate a geometric model (e.g., a CAD model) of the IVC filter
9: Virtually place the geometric model of the IVC filter in the smooth surface mesh of the IVC and deform the legs and arms of the IVC filter by simulating the IVC filter insertion surgery using a superelastic constitutive law for the IVC filter and a linear elastic constitutive law for the IVC.
10: Generate a volume mesh with boundary layer elements using the advancing front algorithm.
11: Perform CFD simulations of the blood flow.

5.1 Image Segmentation

We use the region growing technique for segmentation of our high-quality idealized IVC model CT images. Because the images had very little noise, the edge detection process was rather easy. Figure 5(a) shows the segmentation of the one of the CT images of the idealized model using this technique.

As patients cannot be subjected to high-level radiation, the patient CT images we obtained were of lower resolution. Figure 5(b) shows the segmentation of the one of the patient CT images from the left IVC model using the gradient-based region growing technique. Figure 5(c) shows the segmentation of another patient CT image from the retroaortic model using the intelligent scissors technique. The blue border shows the path traced by the algorithm, and the black square dots are the pixels using which the relevant shortest paths were found. Because the patient images we obtained were not taken at high resolution, we were only able to identify and segment one of the two renal veins in each of our patient IVC models. The renal veins are upstream of the IVC filter, and, thus, the results from our CFD simulations of blood flow using these volume meshes should not be significantly affected due to the absence of one renal vein from each IVC model.

5.2 Surface Mesh Generation

After segmentation of the images, we generate a surface mesh of the IVC model using the marching cubes algorithm. Figure 6 shows the surface meshes generated

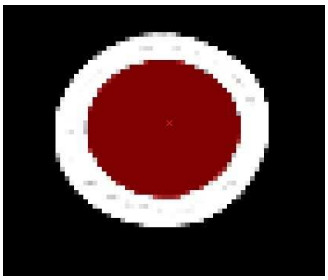

(a) Region growing method segmentation

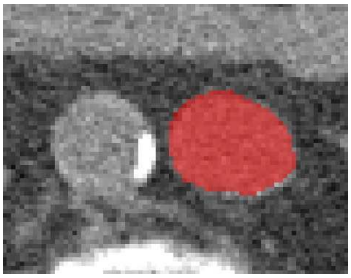

(b) Gradient-based region growing method segmentation

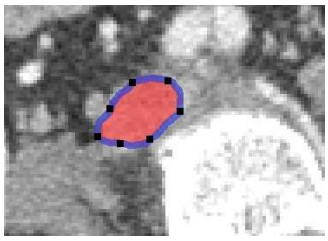

(c) Intelligent scissors segmentation

Fig. 5 Image segmentation of various patient CT images using the region growing method, gradient-based region growing method, and the intelligent scissors method: (a) idealized IVC model, (b) left IVC model, and (c) retroaortic IVC model.

for the three models, i.e., the idealized, left, and retroaortic IVC models generated using the marching cubes algorithm.

The idealized IVC mesh is overrefined, and hence it is reconstructed using Poisson's reconstruction technique and smoothed using the HC-Laplacian smoothing algorithm. The meshes of the left and retroaortic IVC models are also smoothed using this algorithm. Figures 7(a) and (b) show the overrefined mesh of the idealized model and the reconstructed and smoothed mesh of the same model, respectively. Figures 8(a) and (b) show the unsmoothed and final smoothed meshes of the retroaortic IVC model, respectively.

5.3 Virtual IVC Filter Placement

Virtual placement of the IVC filter was performed as described in Section 4.5. Figure 9 shows the deformed filter and the deformed IVC surface meshes. Since arteries are less elastic than veins, we did not see a major deformation in the IVC due to the forces applied by the IVC filter.

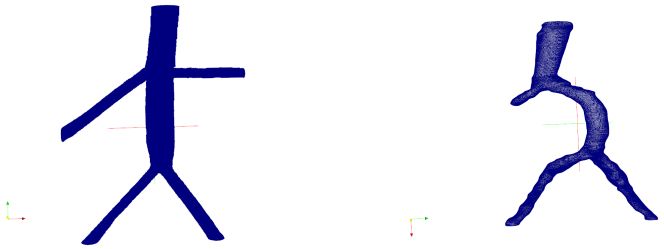

(a) Idealized IVC model (b) Left IVC model

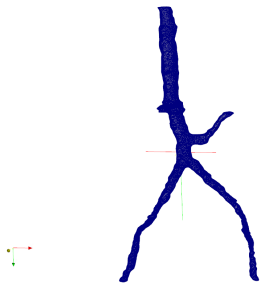

(c) Retroaortic IVC model

Fig. 6 Surface meshes of the three IVC models on which the blood flow simulation were carried out: (a) idealized IVC model, (b) left IVC model, and (c) retroaortic IVC model.

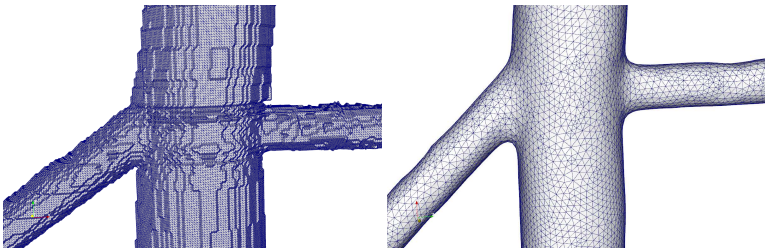

(a) original mesh (b) reconstructed and smoothed mesh

Fig. 7 Mesh reconstruction and smoothing: (a) the original mesh of the idealized model constructed using the marching cubes algorithm. (b) the mesh is reconstructed using the Poisson equation-based algorithm and smoothed using the HC-Laplacian algorithm.

5.4 Volume Mesh Generation

In each of our volume meshes, we generated 10 boundary layers composed of prismatic elements. The initial boundary layer thickness is set to 0.00005 meters, and the geometric ratio by which the thickness increases is set to 1.1. After the boundary layer elements are constructed, tetrahedral and pyramidal elements are generated in the interior of the domain and added to the volume mesh. The quality of the elements are then improved using local reconnection (i.e., edge swaps and face swaps)

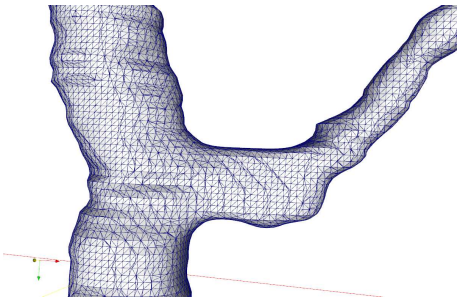

(a) original mesh

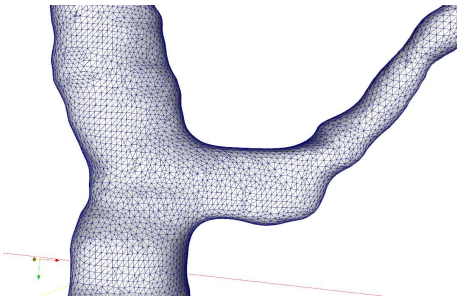

(b) smoothed mesh

Fig. 8 The original mesh of the retroaortic IVC model constructed using the marching cubes algorithm. The mesh is smoothed using the HC-Laplacian algorithm. (a) original mesh, (b) smoothed mesh.

subject to min-max type quality criteria in which the quality of the worst element improved by targeted local reconnection operations. A cut-away view of each of the volume meshes for the three IVC models are shown in Fig. 10.

5.5 Computational Fluid Dynamics

As shown in Figure 11, blood flow in the IVC is quite complex, consisting of vortical structures downstream of the iliac veins, where mixing of the inflow occurs. Based on the present CFD results, f or steady flow at physiologically-realistic flow rates, blood flow in the anatomically-accurate models is less disturbed, consisting of less separated flow, at the level of the IVC filter compared to the idealized model. Such differences in flow patterns may significantly affect clot capture and optimal IVC filter location. Additionally, since such disparate flow patterns likely occur in different patient anatomies, this suggests the need for patient-specific modeling of blood flow in the IVC for optimized filter selection and placement.

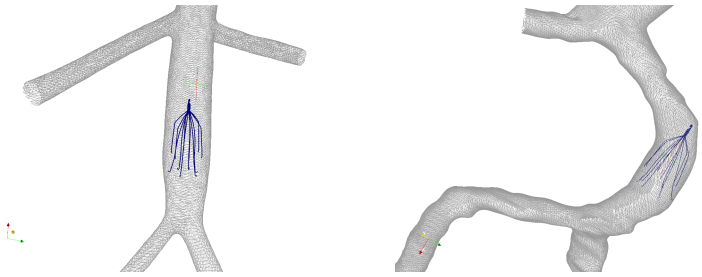

(a) Idealized IVC model (b) Left IVC model

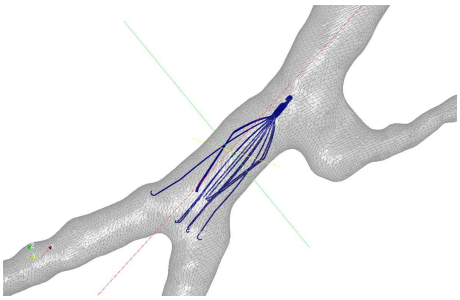

(c) Retroaortic IVC model

Fig. 9 Surface meshes of the three IVC models with the deformed filter inside. The IVC filter undergoes a superelastic deformation, and the IVC undergoes a linear elastic deformation during the filter insertion surgery, which we simulate using a finite element method. (a) idealized IVC model, (b) left IVC model, and (c) retroaortic IVC model.

6 Conclusions and Future Work

We have proposed a computational pipeline approach for generation of patient-specific geometric models and computational meshes of the IVC and IVC filter based on patient CT images and a CAD model of the IVC filter. Our computational pipeline generates anatomically-correct geometric models of the IVC and its surrounding veins by processing patient CT images. In particular, the 2D CT images are segmented and are formed into a 3D geometric model using the marching cubes algorithm. A high-quality surface mesh is then generated on the IVC model. Mesh smoothing is then used to improve the quality of the surface mesh. A geometric model (represented as a surface mesh) of the IVC filter is then created. The IVC filter model is then virtually placed inside the IVC model using a superelastic mesh warping algorithm which simulates the compression and expansion of the IVC filter arms and legs which are composed of nitinol. The corresponding deformation of the IVC is simulated using a linear elastic mesh warping algorithm. The inlet and outlet surfaces of the IVC are rebuilt to be planar and perpendicular to the blood flow as necessary. A volume mesh of the IVC and IVC filter for the left, retroaortic, and idealized IVC models is then generated and is then generated and is

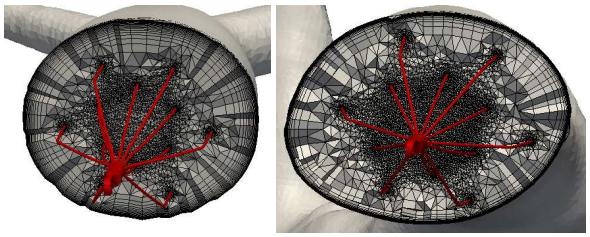

(a) Idealized model (b) Left IVC model

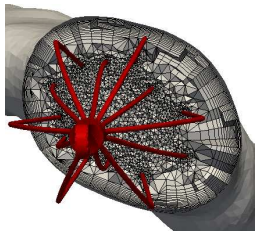

(c) Retroaortic IVC model

Fig. 10 Cut-away views of the volume meshes on the (a) idealized, (b) left, and (c) retroaortic IVC models showing the IVC filter and boundary layer.

used in CFD simulations of blood flow, whereby we illustrate the potential utility of this approach for optimized, patient-specific IVC filter selection and placement for improved treatment of PE.

Our computational pipeline approach is the first semi-automatic technique for generation of patient-specific models and computational meshes of the IVC and IVC filter based on patient CT images of the IVC and surrounding veins and a CAD model of the IVC filter. The novelty in our approach lies in the use of a superelastic mesh warping method to perform virtual implantation of the IVC filter in the IVC. Other virtual implantation techniques, such as those used for implantation of stents, have been solely geometric, as opposed to geometric and physical, in nature. However, the use of physics-based mesh warping techniques allows us to simulate more closely the IVC filter insertion procedure.

We are also the first group to have investigated the effect that patient anatomy has on the performance of an IVC filter. In particular, we investigated the performance of the G2 Express filter in the left IVC, retroaortic IVC, and normal IVC patient anatomies. Earlier work by other researchers has focused on the performance of various IVC filters in the normal IVC anatomy.

The strength of our computational pipeline lies in its ability to be used to investigate the performance of other IVC filters in various IVC anatomies. Because our approach is semi-automatic, several patient-specific geometric models and computational meshes can be generated with less effort by researchers. Previous techniques for generating these involved manual insertion of the IVC filter into the IVC

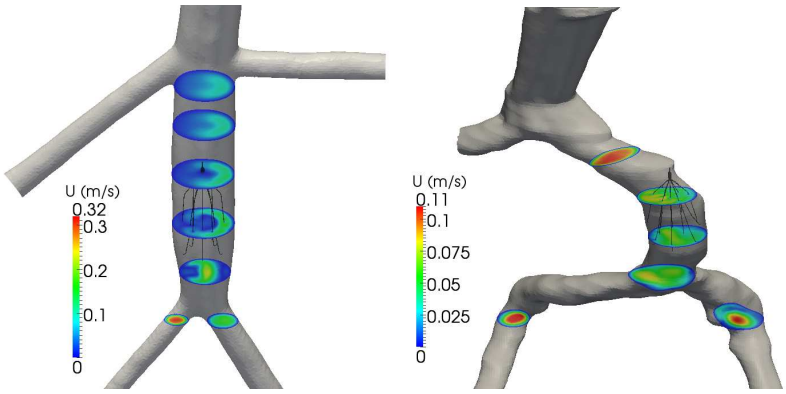

(a) Idealized model (b) Left IVC model

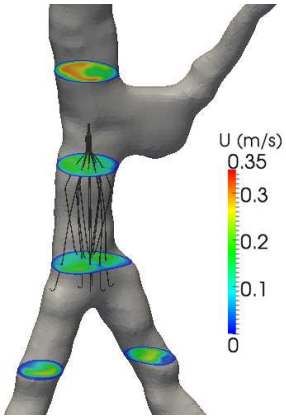

(c) Retroaortic IVC model

Fig. 11 Transverse contours of velocity magnitude extracted from CFD simulation results in the (a) idealized, (b) left, and (c) retroaortic IVC models.

and were more time consuming. Another advantage of our computational pipeline is its flexibility which allows for it to be used to generate patient-specific geometric models and computational meshes for other implanted medical devices composed of nitinol, such as stents or orthodontics.

Future work will focus on automation of the virtual implantation aspect of the computational pipeline, as well as further studies involving patient-specific geometric models and computational meshes of the IVC and IVC filter.

Acknowledgements The authors would like to thank Rick Schraf and Todd Fetterolf for creating the CAD model of the IVC filter. They would also like to thank Katerina Papoulia, of the University of Waterloo, for helpful discussions on the superelasticity computations. The work of the first three authors was supported in part by NSF CAREER Award OCI-1054459. The work of the first, third, fifth, and sixth authors was supported in part by an Institute for Cyberscience grant from The Pennsylvania State University. The work of the third and fifth authors was also supported in part

by a grant from the Grace Woodward Foundation at The Pennsylvania State University. The work of the third author was also supported in part by NSF grant CNS-0720749. The work of the seventh author was supported by a Royal Thai Government Scholarship.

References

1. Abaqus 6.9. http://www.simulia.com/products/abaqus_fea.html
2. Abaqus/CAE User Manual. SIMULIA (2010)
3. Aflr3. http://www.simcenter.msstate.edu/software.php
4. Amira 4.1.2. http://www.amira.com/
5. Amira Reference Guide. Mercury Computer Systems (2009)
6. Anderson, F., Wheeler, H., *et al.*, R.G.: A population-based perspective of the hospital incidence and case-fatality rates of deep-vein thrombosis and pulmonary embolism: The Worchester DVT study. Arch Intern Med **151**, 933–938 (1991)
7. Bah, M., Nair, P., Browne, M.: Mesh morphing for finite element analysis of implant positioning in cementless total hip replacement. Med Eng Phys **31**, 1235–1243 (2009)
8. Baldwin, M., Langenderfer, J., Rullkoetter, P., Laz, P.: Development of subject-specific and statistical shape models of the knee using an efficient segmentation and mesh-morphing approach. Comput Meth Prog Bio **97**, 232–240 (2010)
9. Barber, D., Oubel, E., Frangi, A., Hose, D.: Efficient computational fluid dynamics mesh generation by image registration. Med Image Anal pp. 648–662 (2007)
10. Brountzos, E., Kaufman, J., Venbrux, A., Brown, P., Harry, J., Kinst, T., Klenshinski, S., Ravenscroft, A.: A new optional vena cava filter: Retrieval at 12 weeks in an animal model. J Vasc Interv Radiol **14**, 763–772 (2003)
11. Cebral, J., Lohner, R.: From medical images to CFD meshes. In: Proc. of the 8^{th} International Meshing Roundtable (1999)
12. Cheng, C., Herfkens, R., Taylor, C.: Inferior vena caval hemodynamics quantified *in vivo* at rest and during cycling exercise using magnetic resonance imaging. Am. J. Physiol. Heart Circ. Physiol. **284**(4), H1161–H1167 (2003)
13. Conti, M.: Finite element analysis of self-expanding braided wirestent. Master's thesis, Ghent University, Belgium (2007)
14. Couch, G., Johnston, K., Ojha, M.: An *in vitro* comparison of the hemodynamics of two inferior vena cava filters. J Vasc Surg **31**, 539–549 (2000)
15. Craven, B., Neuberger, T., Paterson, E., Webb, A., Josephson, E., Morrison, E., Settles, G.: Reconstruction and morphometric analysis of the nasal airway of the dog (canis familiaris) and implications regarding olfactory airflow. The Anatomical Record **290**, 1325–1340 (2007)
16. Craven, B., Paterson, E., Settles, G., Lawson, M.: Development and verification of a high-fidelity computational fluid dynamics model of canine nasal airflow. J Biomech Eng **131**, 1–11 (2009)
17. de Putter, S., Laffargue, F., Breeuwer, M., van de Vosse, F., Gerritsen, F.: Computational mesh generation for vascular structures with deformable surfaces. Int J Compute Assis Radiol Surg **1**, 39–49 (2006)
18. Decousus, H., *et al.*, P.L.: A clinical trial of vena caval filters in the prevention of pulmonary embolism in patients with proximal deep-vein thrombosis. New Engl J Med **338**, 409–415 (1998)
19. Dheeravongkit, A., Shimada, K.: Inverse adaptation of a hex-dominant mesh for large deformation finite element analysis. Comput Aided Des **39**, 427–438 (2007)
20. Duerig, T.: Present and future applications of shape memory and superelastic material. In: Proc of Material for Smart Systems, vol. 360, pp. 497–506. Material Reasarch Society (1995)
21. Duerig, T., Pelton, A., Stockel, D.: The use of superelasticity in medicine. In: Fachzeitschrift fur Handle Wirtschaft, Technik und Wissenschaft, Sonderdruck aus Heft, vol. 9/96, pp. 569–574. Metall Verlag-Huthig GanbH (1996)

22. Dyedov, V., Einstein, D., Jiao, X., Kuprat, A., Carsona, J., del Pin, F.: Variational generation of prismatic boundary-layer meshes for biomedical computing. Int J Numer Meth Eng **79**, 907–945 (2009)
23. Fillinger, M., Raghavan, M., Marra, S., Cronenwett, J., Kennedy, F.: *In vivo* analysis of mechanical wall stress and abdominal aortic aneurysm risk. J. Vasc. Surg. **26**, 589–597 (2002)
24. Freitag, L., Ollivier-Gooch, C.: A cost/benefit analysis for simplicial mesh improvement techniques as measured by solution efficiency. Internat J Comput Geom Appl **10**, 361–382 (2000)
25. Frey, P.: Generation and adaptation of computational surface meshes from discrete anatomical data. Int J Numer Meth Eng **60**, 1049–1074 (2004)
26. Frey, P., Sarter, B., Gautherie, M.: Fully automatic mesh generation for 3D domains based upon voxel sets. Int J Numer Meth Eng **37**, 2735–2753 (1994)
27. Gundert, T., Shadden, S., Williams, A., Koo, B.K., Feinstein, J., LaDisa Jr., J.: A rapid and computationally inexpensive method to virtually implant current and next-generation stents into subject-specific computational fluid dynamics models. Ann Biomed Eng **39**(5) (2011)
28. Hao, J., Shen, Y.: Region growing within level set framework: 3-D image segmentation. In: Proc. of the 6^{th} World Congress on Intelligent Control and Automation (WCICA 2006), pp. 10,352–10,355 (2006)
29. Haralick, R., Shapiro, L.: Image segmentation techniques. Comput Vis Graph Image Process **29**, 100–32 (1985)
30. Hartmann, E.: A marching method for the triangulation of surfaces. Visual Comput **14**, 95–108 (1998)
31. Hilton, A., Illingworth, J.: Marching triangles: Delaunay implicit surface triangulation. Tech. rep., University of Surrey (1997)
32. Hoekstra, A., Hoogeveen, Y., Elstrodt, J., Tiebosch, A.: Vena cava filter behavior and endovascular response: An experimental *in vivo* study. Cardiovasc Inter Rad **26**, 222–226 (2003)
33. Holmes, W., Cotton, R., Xuan, V.B., Rygg, A., Craven, B., Abel, R., Slack, R., Cox, J.: Three-dimensional structure of the nasal passageway of a hagfish and its implications for olfaction. The Anatomical Record (2011)
34. Ito, Y., Shum, P., Shih, A., Soni, B., Nakahashi, K.: Robust generation of high-quality unstructured meshes on realistic biomedical geometry. Int J Numer Meth Eng **65**, 943–973 (2006)
35. J. Vollmer R. Mencl, H.M.: Improved Laplacian smoothing of noisy surface meshes. In: Computer Graphics Forum, *Eurographics*, vol. 18, pp. 131–138 (1999)
36. Jr., J.G., Jr., D.G.: Relation between pressure and diameter in main pulmonary artery of man. J. Appl. Physiol. **18**, 557–557 (1963)
37. Katsamouris, A., Waltman, A., Delichatsios, M., Athanasoulis, C.: Inferior vena cava filters: *In vitro* comparison of clot trapping and flow dynamics. J Radiol **166**, 361–366 (1988)
38. Kinney, T.: Update on inferior vena cava filters. J Vasc Interv Radiol **14**, 425–440 (2003)
39. Kunz, R., Haworth, D., Porzio, D., Kriete, A.: Progress towards a medical image through CFD analysis toolkit for respiratory assessment on a clinical timescale. In: Proc. of 2009 International Symposium on Biomedical Imaging: From Nano to Macro, pp. 382–385 (2009)
40. Liu, Y., D'Arceuil, H., He, J., Duggan, M., Gonzalez, G., Pryor, J., de Crespigny, A.: A nonlinear mesh-warping technique for correcting brain deformation after stroke. Magn Reson Imaging **24**, 1069–1075 (2006)
41. Löhner, R.: Progress in grid generation via the advancing front technique. Eng Comput **12**, 186–210 (1996)
42. Lohner, R.: Regridding surface triangulations. J Comput Phys **126**, 1–10 (1996)
43. Lorensen, W., Cline, H.: Marching cubes: A high resolution 3D surface construction method. Compute Graph **21**, 163–169 (1987)
44. M. Kazhdan M. Bolitho, H.H.: Poisson surface reconstruction. In: Proc. of the Fourth Eurographics Symposium on Geometry Processing, SGP, pp. 61–70. Eurographics Association, Aire-la-Ville, Switzerland, Switzerland (2006)
45. Meshlab v1.3.1. http://meshlab.sourceforge.net/
46. Mortensen, E., Barrett, W.: Intelligent scissors for image composition. In: Proc. of the 22nd Annual Conference on Computer Graphics and Interactive Techniques, SIGGRAPH, pp. 191–198. ACM, New York, NY, USA (1995)

47. OpenFOAM website. See http://www.openfoam.com
48. Park, J., Shontz, S., Drapaca, C.: A combined level set/mesh warping algorithm for tracking brain and cerebrospinal fluid evolution in hydrocephalic patients. Invited submission to Image-based Modeling and Mesh Generation, Springer; submitted in October 2011; under review
49. Peiró, J., Giordana, S., Griffith, C., Sherwin, S.: High-order algorithms for vascular flow modelling. Int J Numer Meth Fl **40**, 137–151 (2002)
50. Pelton, A., Stockel, D., Duerig, T.: Medical uses of nitinol. In: Proc. of the International Symposium on Shape Memory Materials, vol. 327–328, pp. 63–70. Material Science Forum Vols. (1999)
51. Persson, P.: Mesh generation for implicit geometries. Ph.D. thesis, MIT (2004)
52. Persson, P.: Mesh size functions for implicit geometries and PDE-based gradient limiting. Eng Comput **22**, 95–109 (2006)
53. Pham, D., Xu, C., Prince, J.: Current methods in medical image segmentation. Annu Rev Biomed Eng **2**, 315–37 (2000)
54. Qian, Z., Yasul, K., Nazarian, G., Vlodaver, Z., Hunter, D., Castenda-Zuniga, W., Amplatz, K.: *In vitro* and *in vivo* experimental evaluation of a new vena cava filter. J Vasc Interv Radiol **5**, 513–518 (1994)
55. Quatember, B., Muhlthaler, H.: Generation of CFD meshes from biplane angiograms: An example of image-based mesh generation and simulation. Appl Numer Math **46**, 379–397 (2003)
56. Rahbar, E., Mori, D., Moore, Jr., J.: Three-dimensional analysis of flow disturbances in inferior vena cava filters. J. Vasc. Interv. Radiol. **22**, 835–842 (2011)
57. Rogers, C., Schief, W., Chow, K.: A novel class of model constitutive laws in nonlinear elasticity: Construction via Loewner theory. Theor Math Phys+ **152**, 1030–1042 (2007)
58. Schmidt, J., Johnson, C., Eason, J., McLeod, R.: Applications of automatic mesh generation and adaptive methods in computational medicine. Springer-Verlag (1994)
59. Sethian, J.: Level Set Methods and Fast Marching Methods: Evolving Interfaces in Computational Geometry, Fluid Mechanics, Computer Vision, and Materials Science. Cambridge Monographs on Applied and Computational Mathematics (1999)
60. Shepherd, J., Johnson, C.: Hexahedral mesh generation for biomedical models in SCIRun. Eng Comput **25**(1), 97–114 (2009)
61. Shewchuk, J.: What is a good linear element? Interpolation, conditioning, and quality measures. In: Proc. of the Eleventh International Meshing Roundtable, pp. 115–126 (2002)
62. Shontz, S., Vavasis, S.: A mesh warping algorithm based on weighted Laplacian smoothing. In: Proc of the 12^{th} International Meshing Roundtable, pp. 147–158 (2003)
63. Siemens NX 6. http://www.plm.automation.siemens.com/en_us/products/nx/
64. Sigal, I., Hardisty, M., Whyne, C.: Mesh-morphing algorithms for specimen-specific finite element modeling. J Biomech **41**, 1381–1389 (2008)
65. Sigal, I., Whyne, C.: Mesh morphing and response surface analysis: Quantifying sensitivity of vertebral mechanical behavior. Ann Biomed Eng **38**, 41–56 (2010)
66. Sigal, I., Yang, H., Roberts, M., Downs, J.: Morphing methods to parameterize specimenspecific finite element model geometries. J Biomech **43**, 254–262 (2010)
67. Silver-Thorn, M.: Predication and experimental verification of residual limb-prosthetic socket interface pressures for below-knee amputees. Ph.D. thesis, Northwestern University (1991)
68. Singer, M., Henshaw, W., Wang, S.: Computational modeling of blood flow in the TrapEase inferior vena cava filter. J. Vasc. Interv. Radiol **20**, 799–805 (2009)
69. Singer, M., Wang, S.: Modeling blood flow in a tilted inferior vena cava filter: Does tilt adversely affect hemodynamics? J. Vasc. Interv. Radiol. **22**, 229–235 (2011)
70. Singer, M., Wang, S., Diachin, D.: Design optimization of vena cava filters: An application to dual filtration devices. J. Biomech. Eng. **132**, 101,006 (2010)
71. Sion, M., Rabkin, D., Kleshinski, S., Kim, D., Ransil, B.: Comparative evaluation of clinically available inferior vena cava filters with and *in vitro* physiologic simulation of the vena cava. J Radiol **189**, 769–774 (1993)

72. Stewart, S., Robinson, R., Nelson, R., Malinauskas, R.: Effects of thrombosed vena cava filters on blood flow: Flow visualization and numerical modeling. Ann Biomed Eng **36**, 1764–1781 (2008)
73. Swaminathan, T., Hu, H., Patel, A.: Numerical analysis of the hemodynamics and embolus capture of a Greenfield vena cava filter. J Biomech Eng **128**, 360–370 (2006)
74. Szczerba, D., McGregor, R., Szekely, G.: High quality surface mesh generation for multi-physics bio-medical simulations. In: Proc. of the 2007 International Conference on Computational Science, vol. 4487, pp. 906–913. Springer Berlin/Heidelberg (2007)
75. Treece, G., Prager, R., Gee, A.: Regularised marching tetrahedra: Improved iso-surface extraction. Comput Graph **23**, 593–598 (1999)
76. Ulrich, D., van Rietbergen, B., Weinans, H., Ruegsegger, P.: Finite element analysis of trabecular bone structure: A comparison of image-based meshing techniques. J Biomech **31**, 1187–1192 (1998)
77. Verma, C., Fischer, P., Lee, S., Loth, F.: An all-hex meshing strategy for bifurcation geometries in vascular flow simulation. In: Proc. of the Fourteenth International Meshing Roundtable, pp. 11–14. Sandia National Laboratories (2005)
78. Wang, S., Singer, M.: Toward an optimal position for inferior vena cava filters: Computational modeling of the impact of renal vein inflow with Celect and TrapEase filter. J. Vasc. Interv. Radiol. **21**, 367–374 (2010)
79. Yamakawa, S., Shimada, K.: Converting a tetrahedral mesh to a prism-tetrahedral hybrid mesh for FEM accuracy and efficiency. In: Proc. of the 2008 ACM Symposium on Solid and Physical Modeling, pp. 287–294 (2008)
80. Yu, Z., Holst, M., McCammon, J.: High-fidelity geometric modeling for biomedical applications. Finite Elem Anal Des **44**, 715–723 (2008)
81. Zachariah, S., Sanders, J., Turkiyyah, G.: Automated hexahedral mesh generation from biomedical image data: Applications in limb prosthetics. IEEE T Rehabil Eng **4**, 91–102 (1996)
82. Zhang, L., Yang, G., Shen, W., Qi, J.: Spectrum of the inferor vena cava: MDCT findings. Abdom Imaging **32**, 495–503 (2007)